



Hybrid simulation of a steel frame with Dissipative Replaceable Link Frames

Giulia Giuliani¹ · Roberto Andreotti¹ · Nicola Tondini¹ 

Received: 9 November 2023 / Accepted: 26 March 2024
© The Author(s) 2024

Abstract

In the last decades, high priority has been given to enhancing the seismic resilience of structures by reducing the damage of structural and non-structural elements after a disaster. In this context, the European Research Fund for Coal and Steel (RFCS) project DISSIPABLE was funded to perform large demonstration tests of steel frames equipped with easily repairable seismic dissipative devices. The paper extensively describes the experimental campaign carried out at the University of Trento on a steel frame equipped with innovative Dissipative Replaceable Link Frame (DRLF) systems, composed of two rigid columns connected by weakened beams at their ends. Hybrid Simulation was employed, enabling to physically test the first floor of the building yet allowing for considering the response of the remaining five floors, which were numerically simulated. A bidimensional frame was tested under increasing seismic intensity levels: Damage Limitation, Significant Damage and Near Collapse limit states. The experimental results proved that the DRLF system was able to dissipate energy and protect the primary elements of the structure from plasticisation. Moreover, the structure's re-centring capability was verified to ensure the components' replaceability. Finally, the calibration of the nonlinear model was performed following the tests, which allowed to develop a high-fidelity model suitable for further numerical investigation.

Keywords Full-scale experimental tests · Hybrid simulation · Steel structures · Seismic devices · Resilient structures · Repairability

1 Introduction

The conventional design of buildings in seismic zones entails energy dissipation in the structural elements. The capacity design, adopted in the main national and international design standards for seismic actions, as the Eurocode 8-1 (CEN 2005a), ensures that plastic hinges form in specific points of the structure to foster a ductile collapse mechanism. For instance, in moment resisting frames (MRF), attention is given to forming plastic hinges at

✉ Nicola Tondini
nicola.tondini@unitn.it

¹ Department of Civil, Environmental and Mechanical Engineering, University of Trento, Via Mesiano 77, 38123 Trento, Italy

the beam ends to protect columns and avoid soft storey mechanisms. In addition, different strategies were proposed to ensure plasticisation of the MRF beams, e.g. weakening the beams at their ends (Plumier 1990; Iwankiw and Carter 1996). As an alternative, studies have been carried out to concentrate the dissipation in partial-strength joints (Castro et al. 2005; Chen et al. 1996; Pucinotti et al. 2015; Tondini et al. 2018). Although these strategies allow for designing structures capable of dissipating energy under seismic loading, they do not guarantee ease of repair after an earthquake. This results in economic losses due to the long-term downtime of the structure. Moreover, buildings designed according to these approaches may undergo significant damage, whose repair work is often not feasible or too expensive. Therefore, reducing damage to structural and non-structural elements after a disaster is fundamental for costs and functionality. Thus, partial-strength joint solutions with low damage were proposed (Francavilla et al. 2020; Latour et al. 2011). Slit dampers applied to MRF (Oh et al. 2009) and eccentrically braced frames (EBF) showed beneficial hysteretic behaviour (Chan and Albermani 2008). At the same time, focus has been given to solutions that can limit damage and guarantee replaceability after seismic events to enhance structural resilience (Wang et al. 2020).

In this context, this work extensively describes the experimental campaign carried out at the University of Trento on a steel frame, whose seismic lateral-resisting system is composed by a “Dissipative Replaceable Link Frame” component, which consists of two rigid columns connected by locally weakened beams. The objective is to provide experimental evidence of large energy dissipation capability and ease of repair of steel structures equipped with such dissipative components. The DRLF is a structural solution that can be referred to as a Linked Column Frame (LCF) and it was called as such in the Research Fund for Coal and Steel DISSIPABLE project (Kanyilmaz et al. 2022). Several authors have extensively studied LCF systems over the last few decades and they involve connecting steel columns with replaceable links that act as fuses (Dusicka and Iwai 2007; Fortney et al. 2007; Lopes et al. 2012). These studies demonstrated the effectiveness of such solutions in dissipating energy and protecting the main structure from damage. In analogy with EBF, LCF systems dissipate energy in the beam links by shear. Conversely, in the present study, energy dissipation occurs in reduced beam sections (RBS) by bending moment, for which geometric rules that avoid shear-bending interaction are employed (Vayas 2017). In addition, Montuori et al. (2023) proposed an effective design procedure based on the Theory of Plastic Mechanism Control (Mazzolani and Piluso 1996). Malakoutian et al. (2013) conducted a comprehensive study on the seismic behaviour of the LCF system coupled with a moment-resisting frame. The analyses proved that the devices have excellent energy dissipation capabilities. However, the study also showed that the structural frame cannot be rapidly repaired for high seismic hazard levels. Therefore, while the devices effectively prevent structural collapse, they do not guarantee efficient repairability of the structure. In this work, gravity beams were hinged to the columns to enhance the structural resilience and post-earthquake recovery, preventing their participation in the dissipative behaviour and possible yielding. Although theoretical models and simulations provide valuable insights, only a limited number of experimental tests have been conducted on full-scale frames (Lopes et al. 2014). Additionally, the actual replaceability of beam links within these structures has not yet been investigated. On these premises, this paper reports the results of an experimental campaign on a full-scale frame, which also demonstrates the actual repairability of the structure. Another significant aspect of the project is the use of the Hybrid Simulation testing technique, which allows the test of large-scale structures by physically reproducing only a meaningful portion in

the laboratory whilst numerically simulating the remainder. Hybrid Simulation (HS) was proposed in the early '70 (Nakashima 2020) and has been successfully applied and validated since then in the seismic engineering field (Abbiati et al. 2015; Del Carpio Ramos et al. 2016; Di Benedetto et al. 2020). Nevertheless, its use has been extended in recent developments to other fields, e.g., fire engineering (Sauca et al. 2018; Abbiati et al. 2020). As a result, only the structure's ground floor was physically tested in the laboratory, whilst the remainder was numerically simulated. Bidimensional frames, representative of a 3D case study, were tested under different seismic intensity levels: Damage Limitation (DL), Significant Damage (SD) and Near Collapse (NC). The aim was to demonstrate the elastic behaviour of the structure expected for the DL limit state, as well as the stable hysteretic behaviour and the replaceability of the dissipative components at SD limit state, at which they should protect the irreplaceable parts from yielding.

The motivation for such tests lies in the DISSIPABLE project that was funded to provide experimental evidence of large energy dissipation capability and ease of repair of steel structures equipped with innovative dissipative components by means of large-scale demonstrative tests. Three different components were examined, namely the "Dissipative Replaceable Braced Connections" (DRBrC), the "Dissipative Replaceable Link Frame" (DRLF) and the "Dissipative Replaceable Beam Splices" (DRBeS), which were named after the INERD, FUSEIS type 1 and FUSEIS type 2 connections (Valente et al. 2016), respectively. They were the result of a design improvement of components developed in previous RFCS projects, i.e., INERD project (Plumier et al. 2006) and FUSEIS project (Castiglioni et al. 2013). The monotonic and the cyclic behaviour of these devices were investigated at the component level; however, experimental evidence of the behaviour of structures equipped with such components under real earthquake conditions still needs to be provided. In Andreotti et al. (2023a, b), the outcomes of the tests on full-scale specimens equipped with DRBeS and DRBrC components are respectively presented, whilst this work focuses on the experimental campaign carried out on a steel frame equipped with the DRLF component.

The paper is organised as follows: a brief description of the dissipative component under investigation is given in Sect. 2; in Sect. 3 the numerical models of both the component and the building prototypes are reported, whilst the description of the ground motion selection is presented in Sect. 4. The description of the hybrid simulation procedure is presented in Sect. 5; whereas in Sect. 6 the experimental test results are described. The calibration of the numerical model is reported in Sect. 7, while Sect. 8 draws some conclusive remarks.

2 Description of the dissipative replaceable link frame (DRLF) system

The dissipative replaceable link frame is a lateral-resisting system conceived to be used in the external frames of a steel or a steel–concrete building. It comprises two columns connected by multiple beams, making the system a Vierendeel beam (Fig. 1). The beam links work mainly in bending or shear, depending on the span-to-height ratio, whilst the columns are subjected to strong axial force components (Vayas 2017). The beam is typically weakened at the ends to force the formation of the plastic hinges at those locations. For this system, replaceability is guaranteed by means of bolted connections between the devices and the columns. Moreover, the beam links are not

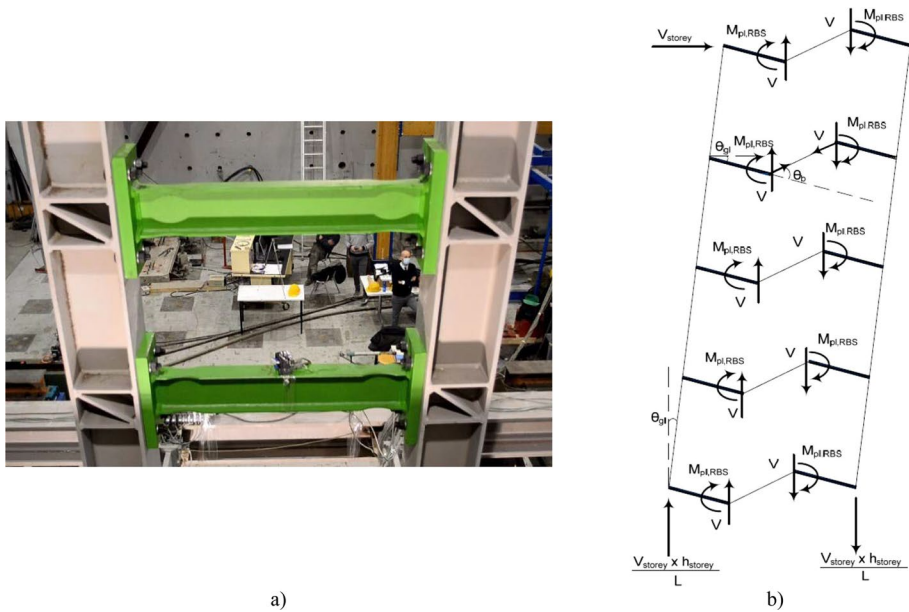


Fig. 1 DRLF system configuration: **a** link beams and **b** mechanical behaviour (Vayas 2017)

part of the gravity load-carrying system. In the tests performed at the University of Trento, IPE sections were employed as beam links and weakened by reducing the gross section in accordance with Eurocode 8-3 (CEN 2005b).

2.1 Numerical modelling of the DRLF component

In the first stages of the work, a preliminary modelling of the DRLF component was performed. Then, after the tests, the numerical model was calibrated, as shown in Sect. 7. In greater detail, the DRLF component was numerically modelled in the finite element (FE) software OpenSees (McKenna et al. 2006). The model is shown in Fig. 2, where the nonlinear part representing the reduced beam sections (RBSs) was modelled with the "TwoNode-Link" element, whilst the remaining parts were modelled through elastic beam elements with the properties of the gross section. To avoid additional flexibility, the model included a rigid link of length equal to half of the column section height at both ends of the beam. The rigid link reproduced the moment-resisting joint between the beam and the column. Moreover, this way of modelling allowed to model the DRLF beam link with the actual physical length (Vayas 2017).

The nonlinear rotational part of the DRLF component was modelled with the Bouc–Wen (Wen 1976) model. The parameters were determined by means of the tool Multical (Chisari et al. 2017), by minimising the difference between a 3D numerical model developed in ABAQUS (Smith 2009) and the beam model developed in OpenSees in terms of energy dissipation and monotonic envelope, as shown in Fig. 3. The dissipated energy differences are 0.9%, 0.4% and 0.1% for the IPE160, IPE140 and IPE100 profiles, respectively. To guarantee a uniform dissipative behaviour along the structure height, three different sections were employed in the prototype model of the building, namely IPE 160, IPE 140 and IPE 100.

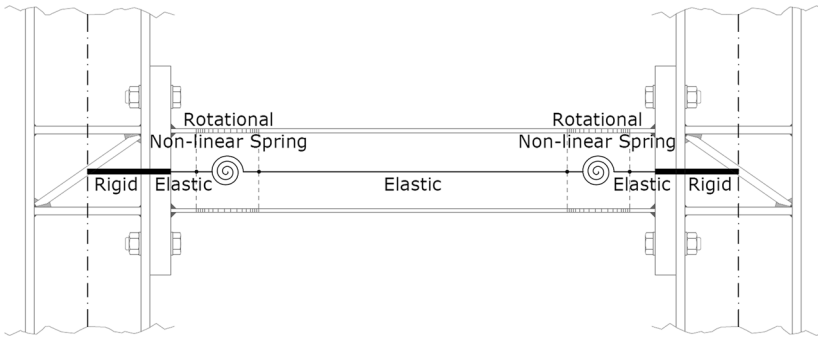


Fig. 2 Beam link numerical model

3 Design of the building prototype structure

The prototype building under investigation comprised two spans in the transversal X-direction, three spans in the longitudinal Y-direction and six stories along the height (Z-direction). Due to laboratory constraints, the span length was 4.275 m, while the

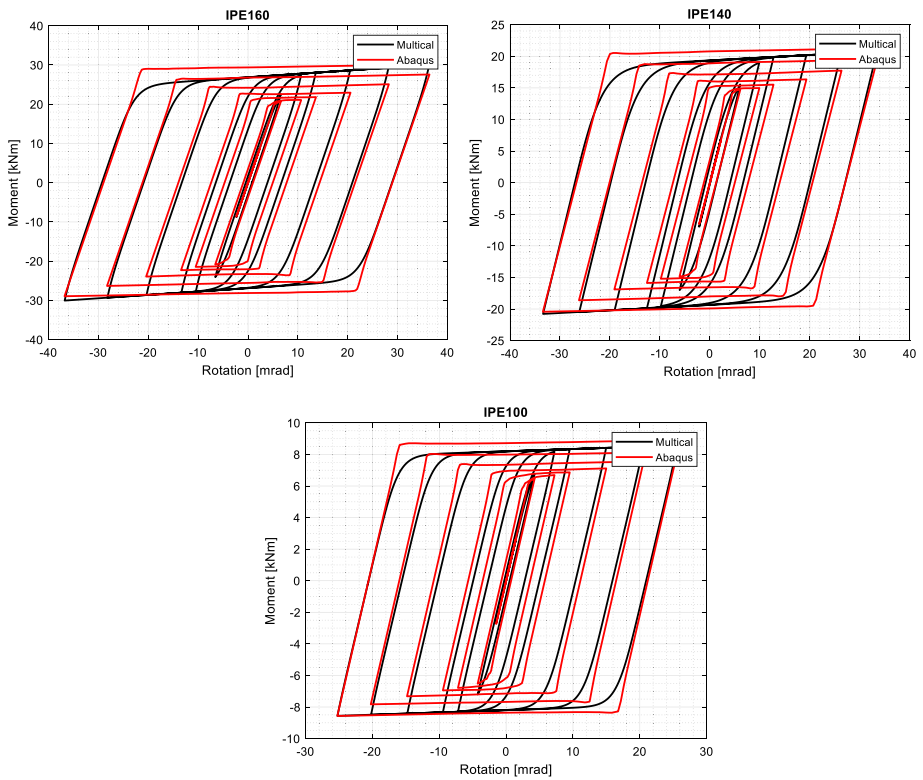


Figure 3. RBSs numerical modelling

Fig. 3 RBSs numerical modelling

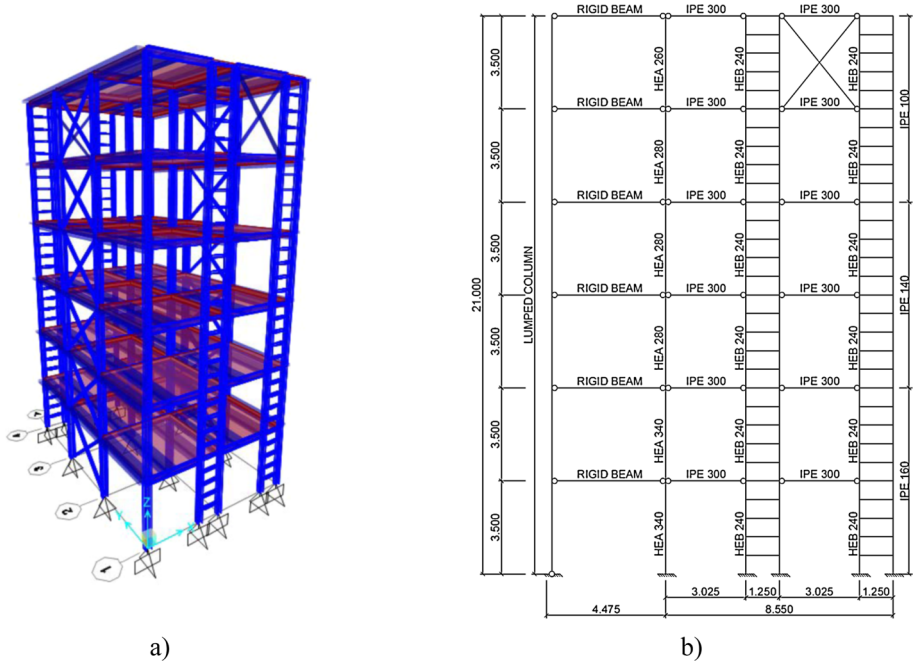


Fig. 4 Case study building: **a** SAP2000 model; **b** 2D model in the direction of the DRLF system. Dimensions in m

Table 1 DRBrC component dimensions in millimetres and element profiles along longitudinal direction

Floor	Pin diameter	Column	Beam	Brace
1–2	45	HEA340	IPE300	HEA140
3–4	40	HEA280	IPE300	HEA120
5	35	HEA280	IPE300	HEA120
6	35	HEA260	IPE300	HEA100

inter-storey height was equal to 3.5 m. In the Y-direction, the lateral-resisting system consisted of two external braced frames equipped with Dissipative Replaceable Bracing Connections. In the X-direction, two parallel DRLF systems were employed and coupled at the top floor by bracing elements (see Fig. 4a) to increase the building stiffness and comply with the deformability limits. As depicted in Fig. 4a, fixed column bases were considered in the direction of the DRLF system, whilst the columns were pinned in the direction of the DRBrC system. Table 1 collects the dimensions of the building dissipative components and structural members along the DRBrC system direction. The static design was performed according to Eurocode 3-1-1 (CEN 2005c), whilst for the seismic design Eurocode 8-1 (CEN 2005a) and Eurocode 8-3 (CEN 2005b) prescriptions were adopted, as suggested by Pinkawa et al. (2017). The structural seismic design was performed by means of linear dynamic analysis of the 3D building developed in SAP2000 (CSI 2019). Member profiles and component dimensions are depicted in Fig. 4b. The deck was composed of a 150 mm high concrete slab with a 55 mm high

Table 2 Modal properties

Mode	OpenSees periods (s)	SAP2000 periods (s)	Error (%)	Participant mass along X (%)	Participant mass along Y (%)	Participant mass along Z (%)
1	1.52	1.49	2	79	0	0
2	1.01	1.00	1	0	71	0
3	0.87	0.84	1	0	0	73

steel sheeting. The steel grade for all the non-dissipative members was S355, whilst for the dissipative components, i.e., IPE profiles that constitute the beam links, S235 steel grade was employed.

Moreover, since a nonlinear model of the numerical substructure was needed for the experimental tests, the building was also modelled in OpenSees, including the nonlinearities of the DRLF system, as described in Sect. 2. In contrast, all other structural members were modelled with elastic beam elements. The comparison between the SAP2000 and the OpenSees models in terms of modal properties is reported in Table 2, where a very good agreement is highlighted.

Pushover and nonlinear time-history analyses were performed to investigate the inelastic behaviour. In this respect, accelerograms at Significant Damage (SD) and Near Collapse (NC) limit states were employed. Figure 5 shows the hysteretic behaviour of RBSS installed in the building subjected to one SD accelerogram. For brevity, only the moment-rotation diagrams at the floor level of the first frame are presented here. The structure experienced large and uniformly distributed hysteretic behaviour, except for the 6th floor, where the components remained almost elastic due to the braces, which provided additional stiffness (see Fig. 5).

Since the experimental tests were performed on 2D frames, reducing the 3D numerical model to a 2D frame and, successively, to a 2D substructured frame that comprised only the numerical substructure was necessary. Hence, only one frame comprising the DRLF system was modelled, and, given the building layout, half of the mass was considered. Moreover, the effect of one internal gravity frame was accounted for by means of a lumped column (Flores et al. 2016), whose modulus of inertia was calculated, floor by floor, as the sum of the modulus of inertia of all the columns belonging to the gravity frame. As a result, the analysed frame is depicted in Fig. 4b.

Then, a further substructuring step was performed to consider the actual laboratory configuration. A maximum of two actuators can be simultaneously controlled. Moreover, only the horizontal degree of freedom can be effectively controlled in the laboratory. On these premises, preliminary analyses were conducted to obtain consistent results between the 2D frame and the 2D substructured frame (SF) shown in Fig. 6, simulating the actuators' presence by continuity constraints between the numerical and experimental substructures. In this respect, the optimal position of the second actuator was assessed by changing the location of the hinge along the column height of the second floor. The mid-height position, which represents the contraflexure point with good approximation, was the location that minimised the difference between the 2D monolithic and the 2D substructure frames. Moreover, the P- Δ effects were also investigated and relevant comparisons showed that discrepancies were negligible. In greater detail, Fig. 7 compares the top floor displacement during the strong motion phase at the near collapse limit state using both linear and P- Δ formulations. The results showed that considering second-order effects did not improve the

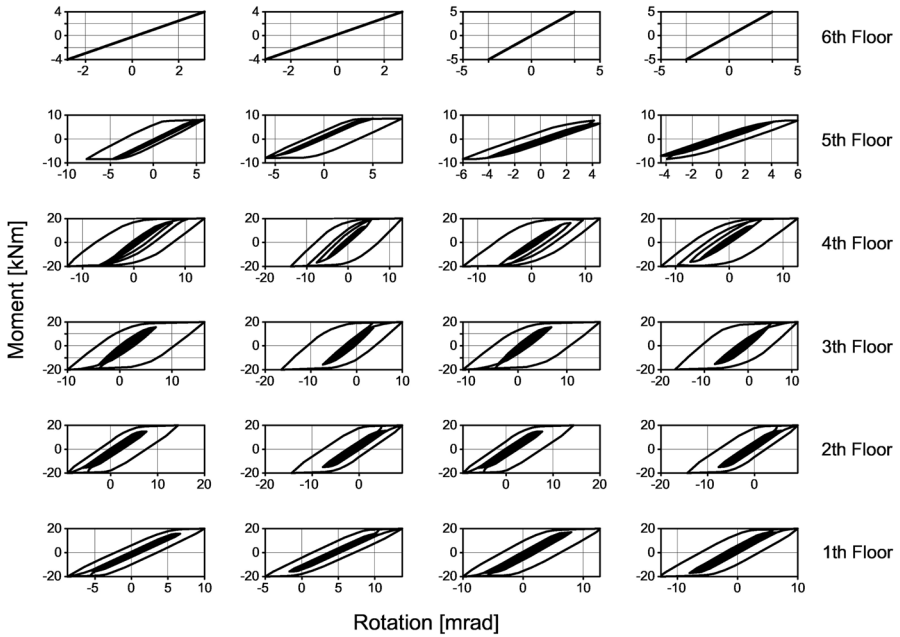


Fig. 5 Hysteretic behaviour of RBSs at SD limit state

accuracy of the results. Thus, it was decided not to apply the axial loads to the columns and the vertical loads to the beams in the physical substructure.

The comparison between the modal properties of the 3D building, the 2D frame and the 2D substructured frame in the direction of the DRLF are reported in Tables 3, 4, 5. In

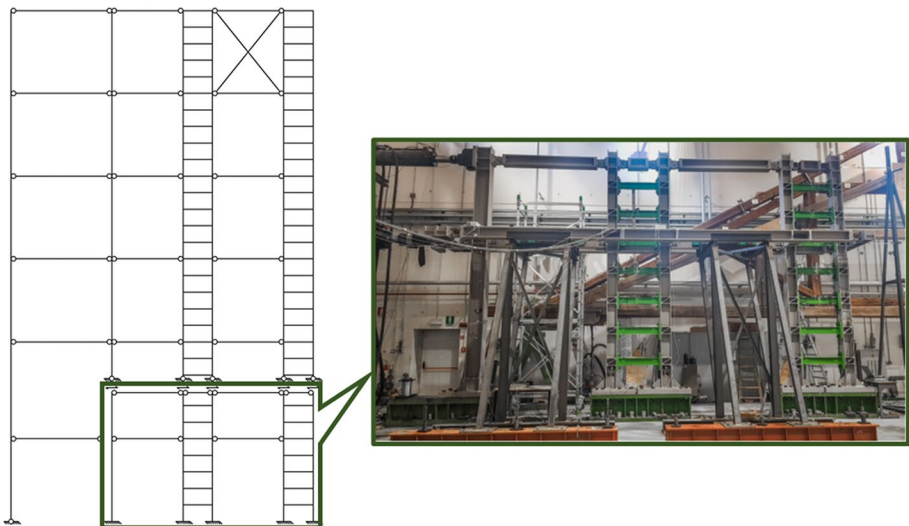


Fig. 6 2D Substructured Frame

Fig. 7 Top floor displacement at the near collapse limit state

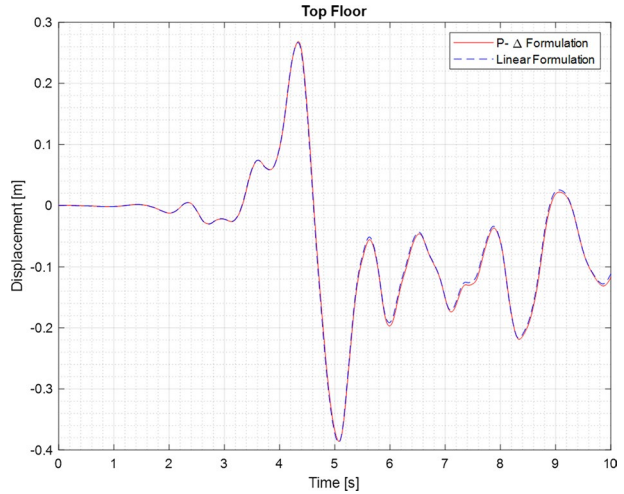


Table 3 Comparison of the modal properties between 3D building, 2D frame and 2D substructure frame

Mode	3D periods (s)	2D periods (s)	SF periods (s)	Error 3D-2D (%)	Error 2D-SF (%)
1	1.52	1.55	1.39	2	11
2	0.38	0.39	0.40	1	1
3	0.19	0.19	0.19	1	0

Table 4 MAC matrix between 3D building and 2D frame

		2D frame		
		Mode 1	Mode 2	Mode 3
3D Building	Mode 1	1	0	0
	Mode 4	0	0.99	0
	Mode 8	0	0	1

Table 5 MAC matrix between 2D frame and 2D substructured frame

		2D substructured frame		
		Mode 1	Mode 2	Mode 3
2D Frame	Mode 1	1	0	0
	Mode 2	0	1	0
	Mode 3	0	0	0.99

Tables 4 and 5, the modal assurance criterion (MAC) (Pastor et al. 2012) was computed to investigate possible discrepancies between the mode shapes. Very good agreement, both in terms of periods and mode shapes, can be observed.

As shown in Fig. 8, the pushover analyses highlight that the nonlinear behaviour of the 2D frame and the 2D substructured frame agree well after the yielding of the devices, whilst the initial stiffness turns out to be different due to the discontinuity and the vertical restraint on the numerical substructure.

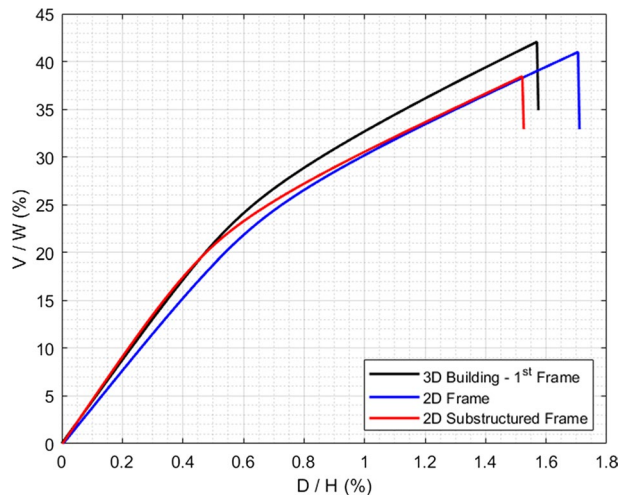
Given the large number of degrees of freedom (DoFs), to reduce the computational burden during the hybrid simulations, the DRLF model was reduced to a simplified one. As shown in Fig. 9, condensation of the DoFs was performed under the assumption of the structure's shear-type deformation, leading to considering only seven horizontal degrees of freedom. These DoFs represented the displacements at each floor level plus the one at the substructuring level. Lumped masses, connected by means of nonlinear shear springs, were located on each DoF. To calibrate the nonlinear spring parameters, a displacement control analysis was performed by imposing a cyclic displacement at the top floor of the reference model. The calibration results are reported in Fig. 10, which highlights good agreement between the reference model and the model used in the experimental tests.

4 Ground motion selection

The tests were conducted at three limit states, namely Damage Limitation (DL), Significant Damage (SD) and Near Collapse (NC) limit states. For each of them, an accelerogram was selected within a set of seven natural ground motions. The selection criteria were (i) the spectral compatibility in accordance with Eurocode 8-1 (CEN 2005a); (ii) the minimisation of the errors between the 2D monolithic and the 2D substructured frame; (iii) the uniformity of inelastic behaviour in the frame at the SD and NC limit states. As a result, Fig. 11 and Table 6 report the selected accelerograms and the related spectra, where the scaling factor was adopted to ensure spectral compatibility.

As shown in Fig. 11c, the selected ground motion for NC limit state was a pulse-like record and did not respect the imposed limits within the range of periods indicated by

Fig. 8 Pushover comparison



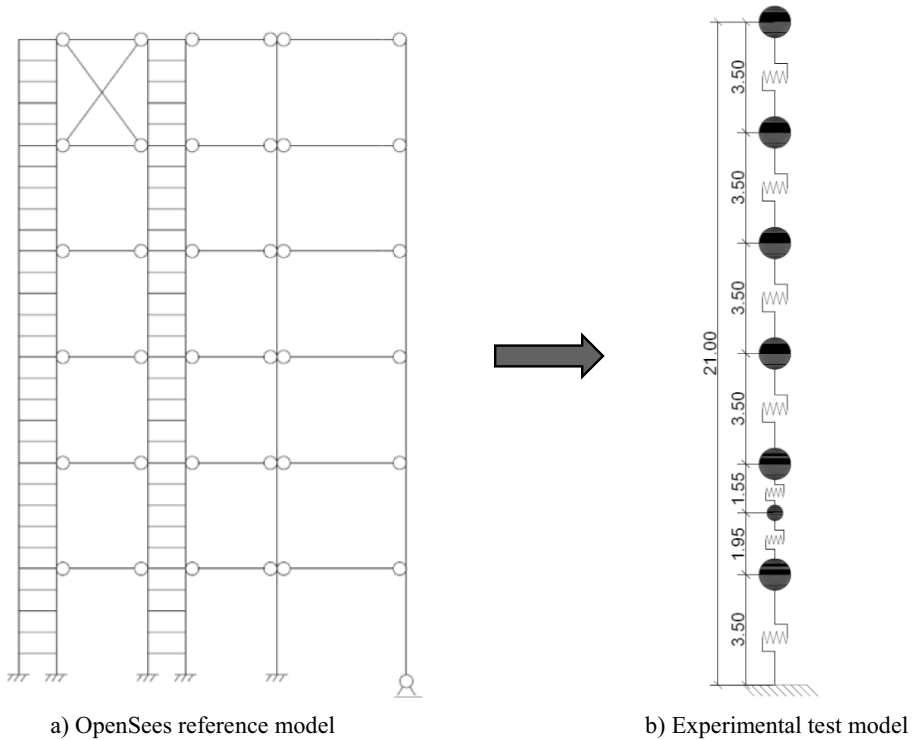


Fig. 9 Model reduction. Dimensions in m

the draft of the new Eurocode 8-1C8 (CEN 2018). However, Eurocode 8-1C8 allows for the use of such accelerograms, hence it was employed to obtain structural damage substantially different from the one at the SD limit state.

Furthermore, for each selected accelerogram, the difference between the response of the monolithic 2D frame and the 2D substructured frame was assessed by computing the following error measures:

- Percentage error on the total hysteretic energy dissipated by the structure.
- Statistical indicators on bending moment history at the RBS.

The aforementioned error indicators are computed as indicated in Eqs. (1), (2) and (3).

$$\text{Energy Error} = \frac{|E_i - E_j|}{E_j} \tag{1}$$

$$\text{NRMSE} = \frac{\|x_i - x_{j2}\| / \sqrt{N}}{x_{j,\max} - x_{j,\min}} \tag{2}$$

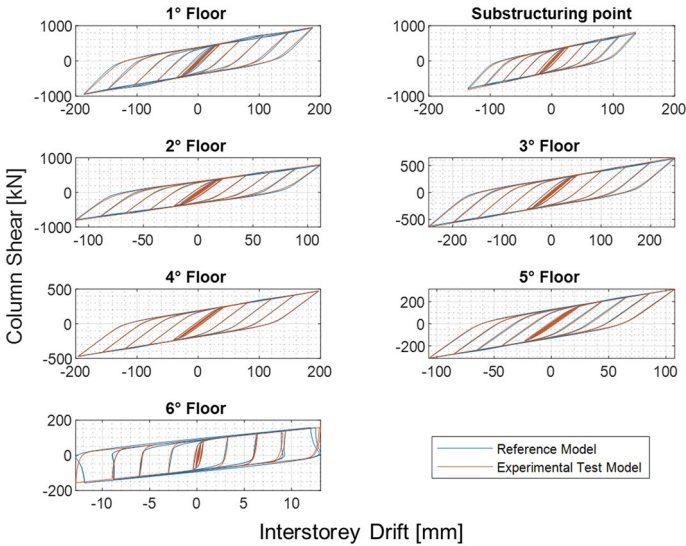


Fig. 10 Comparison between the reference and reduced experimental models regarding inelastic behaviour in the DRLF system

$$NENERR = \left| \frac{\|x_i\|_2 - \|x_j\|_2}{\|x_j\|_2} \right| \tag{3}$$

The energy error in Eq. (1) is the difference between two scalar quantities, i.e., the hysteretic energy dissipated by the DRLF components for the two models, i.e. the sub-structured 2D frame i and monolithic 2D frame j , in which the j dataset is taken as reference. The parameters reported in Eqs. (2) and (3), compare the bending moment evolution in the DRLF components for the two models. NRMSE is sensitive to frequency while NENERR to amplitude (Abbiati 2014). The mean error among all the components for the selected accelerograms are listed in Table 7, whose magnitude is reasonably low.

The structural performance of the frame was evaluated by checking the rotations of RBSs. At the DL limit state all the RBSs attained a maximum rotation lower than the yield rotation, as shown in Fig. 12a. Specifically, the yield rotation was computed using the mean value of the yield strength of an S235 $f_{y,m} = 281.10$ MPa, with a coefficient of variation equal to 0.1 (Hess et al. 2002), according to D.M. 9/1/1996 (Ministero dei Lavori Pubblici 1996). The following values were obtained: 2.15 mrad, 3.19 mrad, 4.92 mrad, respectively for IPE160, IPE 140 and IPE100. Moreover, as illustrated in Fig. 12b and c, a uniform dissipative behaviour was achieved for both the SD and the NC limit states. It should also be highlighted that the higher stiffness given by the bracing system caused smaller rotations of the RBSs located at the top floor.

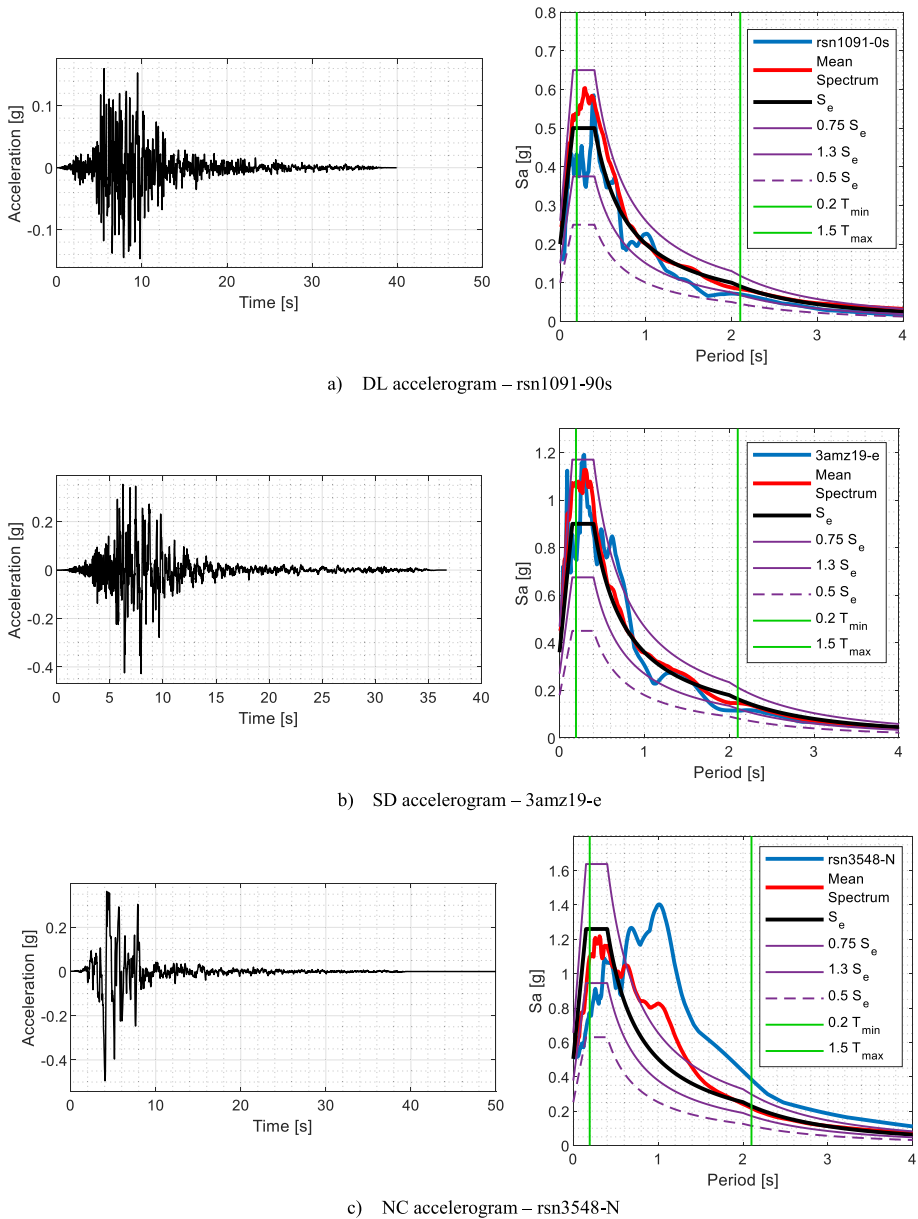


Fig. 11 Selected accelerograms and spectral compatibility

5 Hybrid simulation

The tests were conducted by means of the HS technique, which allows testing a large structure by physically building only part of the structure in the laboratory, which is the physical substructure (PS), whilst the remaining part is numerically simulated, i.e. the numerical substructure (NS). The procedure employed in the experimental campaign

Table 6 Accelerograms

Database record number	Event	Year	Station	M_w	Component	Limit state	Scaling factor
rsn1091	Northridge-01	1994	Vasquez Rocks Park	6.69	South	DL	1.15
3amz19	Central Italy	2016	Pasciano cimitero	6.5	East	SD	1.20
rsn3548	Loma Prieta	1989	Los Gatos—Lexington Dam	6.93	North	NC	1.20

Table 7 Error between monolithic and substructured frame responses. Values in %

Parameters	DL	SD	NC
Energy error	/	57.28	29.09
NRMSE—bending moment	13.55	11.38	4.37
NENERR—bending moment	25.78	15.27	30.46

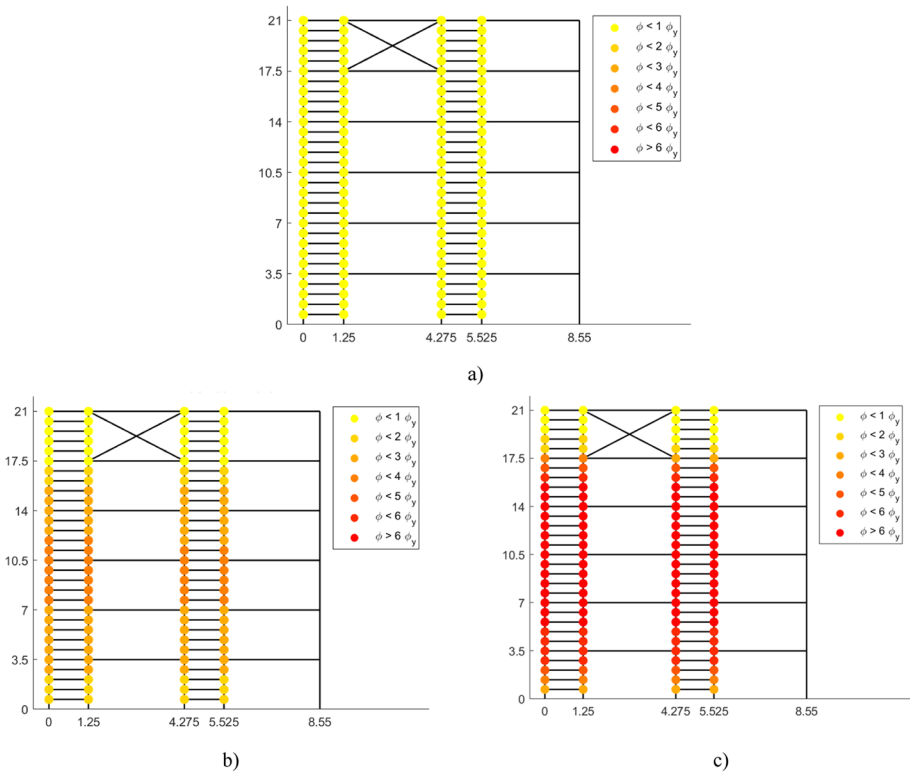


Fig. 12 Maximum RBSs rotation for the selected accelerograms at **a** DL, **b** SD and **c** NC limit state. Dimensions in m

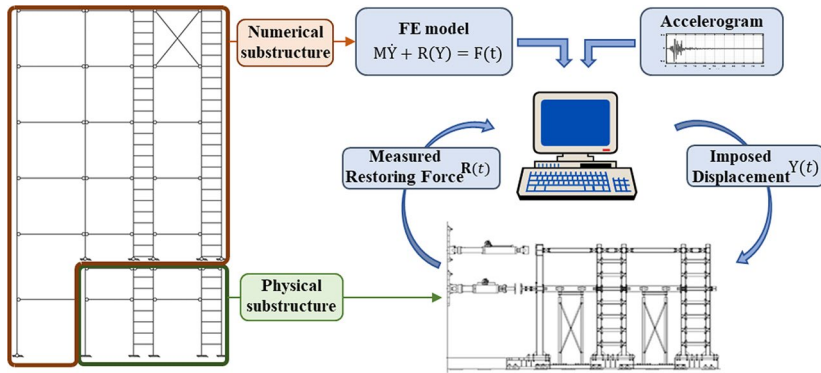


Fig. 13 Conceptual scheme of hybrid simulation

is shown in Fig. 13, and it relies on a partitioned algorithm, the main features of which will be described below. In particular, at each time step, the reaction forces of the structure are measured and sent back to the laboratory PC, where the partitioned algorithm computes the displacements to be imposed on the structure at the next time step by solving the equations of motion which combine the two substructures. Pseudodynamic tests were performed, and the mass contribution of the physical and numerical substructure was only numerically simulated. Moreover, the damping contribution was also numerically accounted for the numerical subdomain, with a damping ratio of 2%, whilst it was not considered in the physical subdomain since is inherent in the nonlinear phenomena. The time-scale factor λ given in Eq. (4) expanded the time scale to avoid considering the inertia forces on the physical substructure. The factor λ is given as the ratio between the time integration step Δt_c used to solve the equations of motion and the wall clock time Δt corresponding to the time interval between two consecutive commands sent by the controller to the actuators (Bursi and Wagg 2009).

$$\lambda = \Delta t_c / \Delta t \tag{4}$$

The value of λ was equal to 50, for the test at DL limit state, and to 100, for both SD and NC tests. A larger λ was employed for the tests where large inelastic behaviour was expected.

Regarding the partitioned algorithm, the G- α algorithm described by Abbiati et al. (2019) was implemented to solve the equations of motion. Briefly, the algorithm rewrites the system of equations of motion in the state space form, which read

$$M\dot{Y} + R(Y) = F(t) \tag{5}$$

where

$$Y = \begin{pmatrix} u \\ v \\ s \end{pmatrix}, M = \begin{pmatrix} I & 0 & 0 \\ 0 & m & 0 \\ 0 & 0 & I \end{pmatrix}, R = \begin{pmatrix} -v \\ r(u, v, s) \\ g(u, v, s) \end{pmatrix}, F = \begin{pmatrix} 0 \\ f(t) \\ 0 \end{pmatrix} \tag{6}$$

u , v and r are the displacement, velocity and restoring force vectors, s is the additional state vector used to model nonlinearities, while I and m are the identity and mass matrices. The

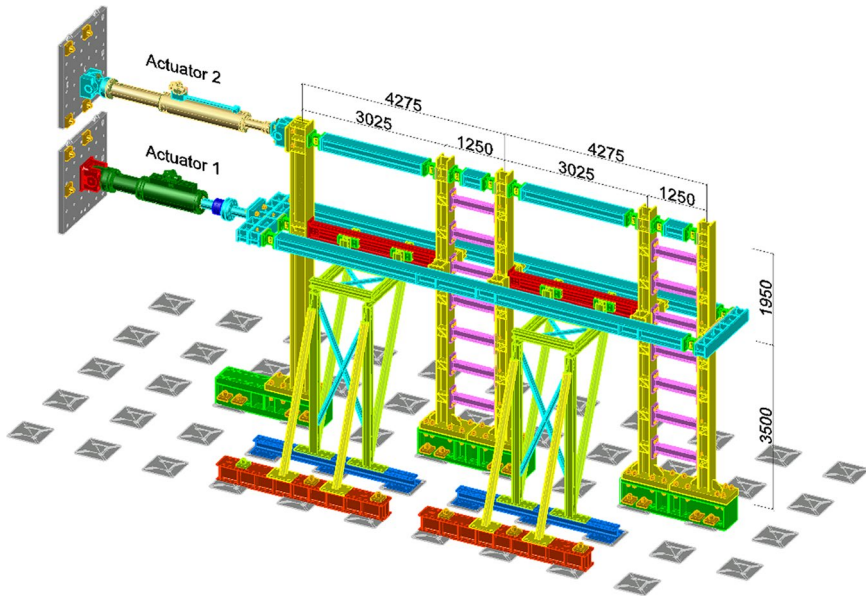


Fig. 14 Experimental test set-up

term $g(u, v, s)$ is the nonlinear function that models the evolution of the additional state vector. As described in Sect. 2, the Bouc–Wen (Bouc 1967; Wen 1976) model was implemented to simulate the evolution of the RBSs nonlinear behaviour (Bonelli and Bursi 2005; Li et al. 2012; Abbiati et al. 2015). In the model, the restoring force reads:

$$r(t) = \alpha ku(t) + (1 - \alpha)kz(t) \quad (7)$$

where α is the ratio between the post-yielding and initial elastic stiffness, k is the initial elastic stiffness and $z(t)$ is the hysteretic displacement whose constitutive law is given as the solution of the following nonlinear differential equation.

$$\dot{z} = \frac{[A\dot{u} - \nu(\beta|\dot{u}||z|^{n-1}z + \gamma\dot{u}|z|^n)]}{\eta} \quad (8)$$

In Eq. (8), A , β , γ and n are parameters that control the shape of the hysteretic loops whilst η and ν govern the main stiffness and strength degradation phenomena, respectively. In the context of the algorithm implementation, the hysteretic displacement $z(t)$ was selected as the additional state vector whilst the differential equation, i.e. Eq. (8), represents the nonlinear function $g(\dot{u}, z)$ which was implemented in the laboratory PC.

As mentioned, only a relevant part of the structure was physically built in the laboratory, whilst the remainder was numerically modelled. The physical and numerical sub-structure response, PS and NS, respectively, were coupled with the partitioned algorithm, which employs Lagrange multipliers. From a physical point of view, the latter represents the interface forces exchanged between NS and PS. Moreover, the compatibility is imposed on the velocity of the interface degrees of freedom by means of the following equation,

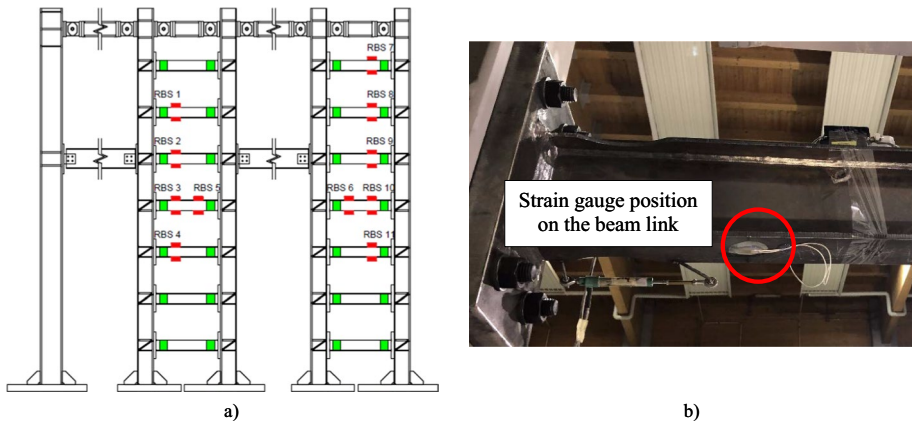


Fig. 15 Strain gauges configuration: **a** instrumentation scheme, **b** sensor position

$$G^{NS} \dot{Y}_{n+1}^{NS} + G^{PS} \dot{Y}_{n+1}^{PS} = 0 \tag{9}$$

where G^{NS} and G^{PS} are the Boolean matrices that localise the interface degrees of freedom on the velocities, \dot{Y}_{n+1}^{NS} and \dot{Y}_{n+1}^{PS} and the state vector first derivative with respect to time. The NS and PS apexes indicate the numerical and physical substructure, respectively.

5.1 HS configuration and instrumentation

As mentioned in Sect. 3, the selected substructured configuration involved the use of two actuators in the test set-up. The physical substructure of the frame, depicted in Fig. 14, was composed of five columns, four of which were part of the DRLF systems that carry the horizontal loads. To impose the same displacement at the top of each column, beams with high axial stiffness were placed at the level of the top actuator. Furthermore, the application of a significant axial force on the device would have affected the response of the beam links. Therefore, two rigid axial beams were laterally installed at the first-floor level, which allowed to replicate the rigid diaphragm effect. In addition, a truss system was adopted to brace the frame laterally and prevent out-of-plane instability.

Figures 15, 16 and 17 depict the instrumentation configuration and the RBS numbering whilst in Table 8 the main characteristics of the sensors are listed. Since it was impossible to instrument all RBSs given the number of available channels, eleven significant sections were selected for their expected dissipative behaviour and instrumented by both strain gauges and displacement transducers. In greater detail, strain gauges were positioned outside the dissipative zone of the DRLF component, in an elastic region near the RBS, to estimate the bending moment according to elastic theory. In this respect, the section's upper and lower edges of the section were instrumented to measure the strain. The curvature could be calculated by assuming plane sections according to Eq. (10)

$$\chi = \frac{\epsilon_{top} - \epsilon_{bot}}{H_{sec}} \tag{10}$$

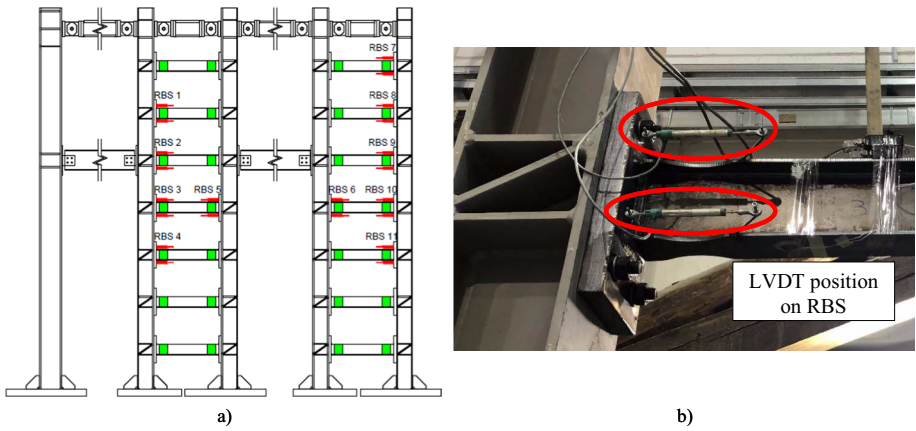


Fig. 16 Displacement transducers configuration: **a** instrumentation scheme, **b** sensor position

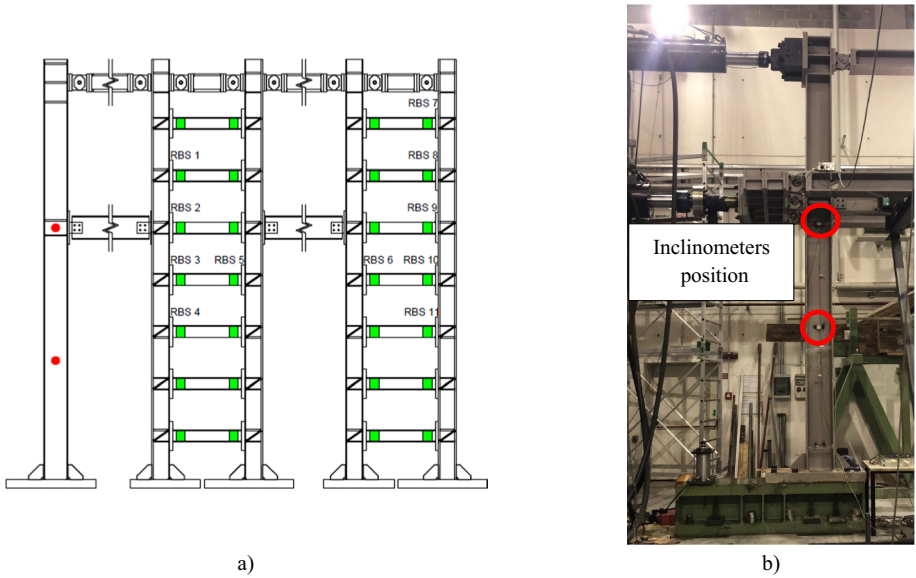


Fig. 17 Inclinerometers configuration: **a** instrumentation scheme, **b** sensor position

Table 8 Instrumentation main characteristics

Strain gauges		LVDT		Inclinometers	
Measuring grid length (mm)	6	Stroke (mm)	± 50	Measuring range (degrees)	± 10
Accuracy (%)	± 1	Accuracy (%)	± 0.1	Accuracy (%)	± 0.1

Table 9 Mechanical properties of S355 steel profiles

Property	HEA 340	HEA 240	IPE 300
Yield strength f_y (MPa)	364	380	434
Ultimate strength f_u (MPa)	553	551	570
Elongation at failure (%)	38	32	27

Table 10 Mechanical properties of S235 IPE160 profile

Property	t = 8 mm	t = 5 mm
Yield strength f_y (MPa)	268.6	250.5
Ultimate strength f_u (MPa)	431.5	426.9
Elongation at failure (%)	36	34

Table 11 Bending capacity of RBS

Yield limit (kNm)	19.82
Plastic resistance (kNm)	22.58

where ϵ_{top} is the strain measured at the top flange, ϵ_{bot} the strain measured at the bottom flange and H_{sec} is the height of the cross section. An estimation of the bending moment on each instrumented section was then obtained by means of Euler–Bernoulli beam theory. In the following formula, I_{beam} is the modulus of inertia of the gross section and E_s is Young’s steel modulus.

$$M = E_s I_{beam} \chi \tag{11}$$

By assuming the prevalence of the seismic actions with respect to the gravity loads on the devices, the bending moment at the reduced beam section was obtained by linear interpolation. Moreover, the rotation of RBSs was calculated from the measurements of the displacement transducers as:

$$\varphi = \frac{\Delta_{top} - \Delta_{bot}}{H_{sec}} \tag{12}$$

where Δ_{top} and Δ_{bot} are the top and bottom relative displacements of the RBSs. Two inclinometers were applied on the first column to calculate the base bending moment and to evaluate whether the column remained in the elastic range.

5.2 Material properties

The actual mechanical properties of all the materials are reported in Tables 9 and 10. The beam links were constructed using welded plates and the capacity proprieties of the reduced beam section, based on the laboratory profile dimensions and actual mechanical characteristics, are listed in Table 11.

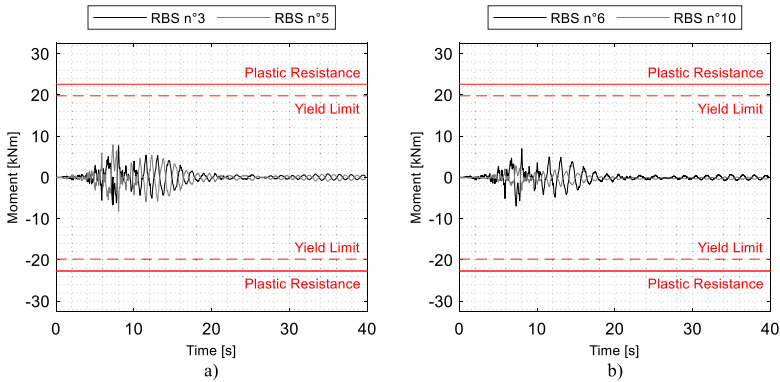


Fig. 18 DL—Bending moment of the RBSs at the floor level, see Fig. 15a

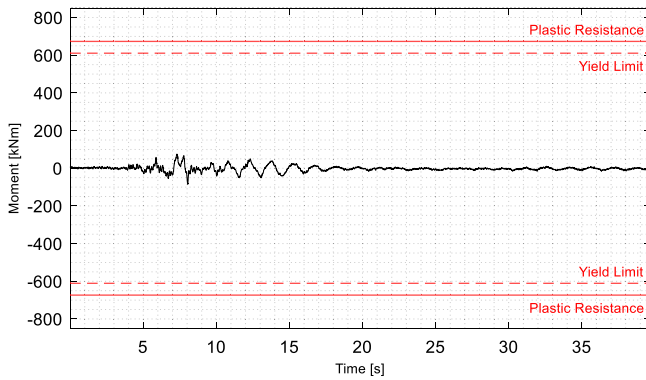


Fig. 19 DL—Bending moment at the base of the first column

5.3 Test procedure

To fully characterise the seismic response of the frame equipped with coupled DRLF systems, a series of hybrid simulation tests at different limit states were carried out in increasing order of intensity. The test programme was conducted as follows:

- 1) Damage Limitation (DL) limit state test. After the test, the elastic behaviour of the dissipative components and of the structural members was checked.
- 2) Significant Damage (SD) limit state test. After the test, the elastic behaviour of the structural members and the inelastic behaviour of the dissipative components were checked.
- 3) The damaged DRLF components were replaced with new ones. The self-centring capacity of the prototype building was verified and the residual interstorey drift was measured. Moreover, the reparability times were computed.
- 4) Near Collapse (NC) limit state test.

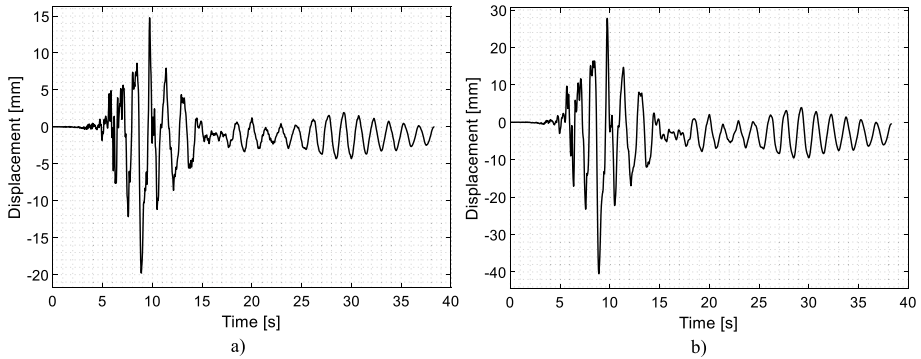


Fig. 20 SD—Actuator displacements: **a** Actuator 1, **b** Actuator 2

6 Hybrid simulation results

6.1 Damage limitation limit state

At the DL limit state, the elastic behaviour of the structure was verified for both the primary elements and the dissipative components. The instrumentation located on the RBSs highlighted that the maximum moment attained during the test was 37.5% of the elastic moment, as can be observed from Fig. 18.

Given that the DRLF system behaves as a cantilever Vierendeel beam and the first column of the frame did not belong to the DRLF system, this column was the one that was subjected to the highest bending moment at its base. Moreover, it was also one of the primary elements that could not be replaced after an earthquake. The column base bending moment was computed based on the inclinometer measurement and elastic theory. As depicted in Fig. 19, the maximum bending moment did not exceed the yield limit, confirming that it remained in the elastic range.

6.2 Significant damage limit state

For the SD limit state, the structure underwent plastic deformation localised on the RBSs of the DRLF links. The results in terms of the two actuators displacement are reported in Fig. 20. The maximum displacement attained at the floor level was of 19.79 mm, which corresponds to an interstorey drift ratio (IDR) of 0.57% whereas the residual displacement after the test was equal to 1.33 mm. This value corresponds to the 0.04% of IDR which demonstrate the high re-centring capability of the structure and, as an important outcome, the ease of replacement of the beam link. Following the test, all beam links were replaced, with an overall repair time corresponding to six working hours of one person, which represents a beneficial outcome in the context of structural resilience. The bending moment history of the first column, depicted in Fig. 21, shows that the yield limit was not exceeded even for the SD limit state, confirming that the column remained elastic, which is another favourable outcome of the project. Given the fact that the structure was designed for the SD limit state, the latter result confirms the DRLF components' capability to protect the frame's irreplaceable parts, i.e., beams and columns, by localising the damage in the RBSs of the beam links.

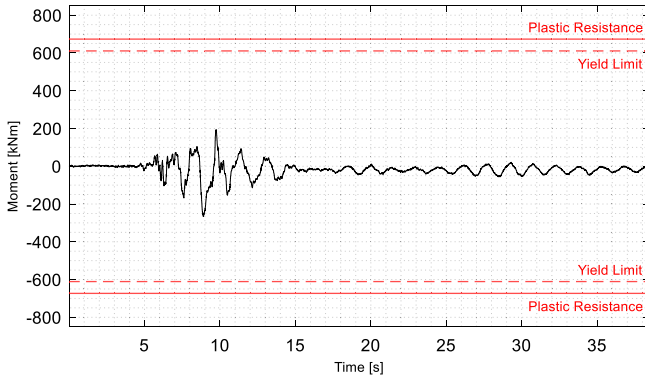


Fig. 21 SD—Bending moment at the base of the first column

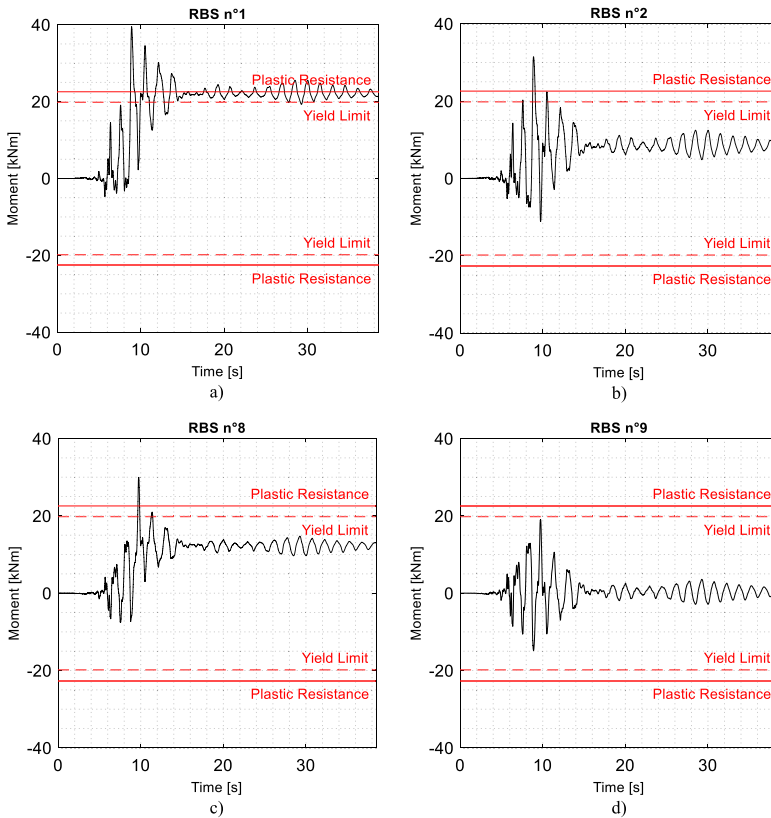


Fig. 22 SD—Bending moment on selected RBSs

The local behaviour of the selected RBSs is reported in terms of bending moment histories. It can be noticed that most of the sections yielded at this intensity level, see Fig. 22a-c; nevertheless, some RBSs remained elastic, Fig. 22d. In Fig. 23, the hysteretic loops of two selected RBSs are reported, and RBS n°4 reached a maximum rotation of 5 mrad. Finally,

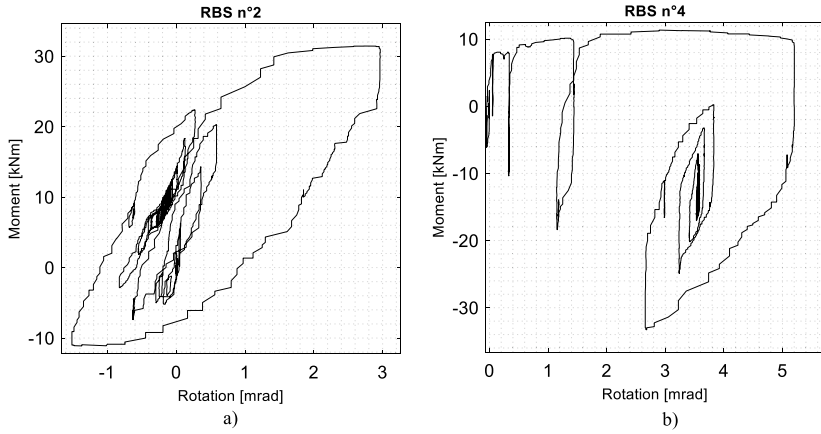


Fig. 23 SD—Cyclic behaviour of selected RBS

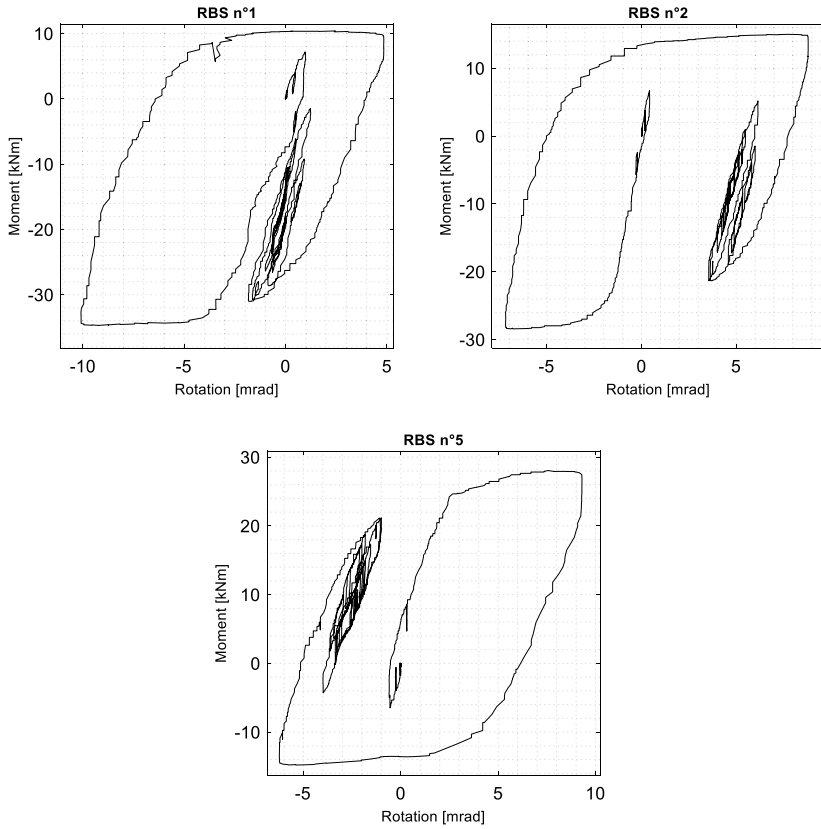


Fig. 24 NC—Cyclic behaviour of selected RBS

Fig. 25 NC—Out-of-plane displacement recorded

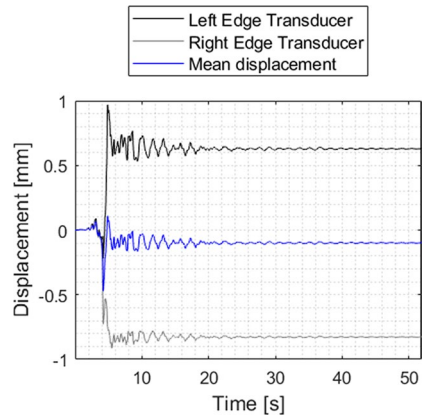


Fig. 26 NC—Bending moment along the two principal axes

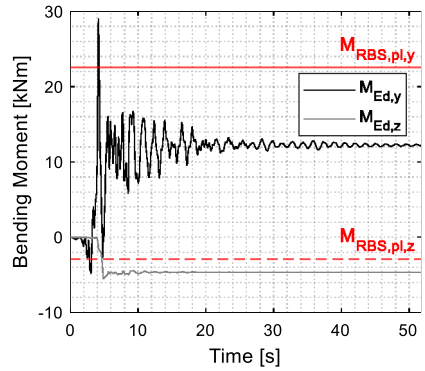
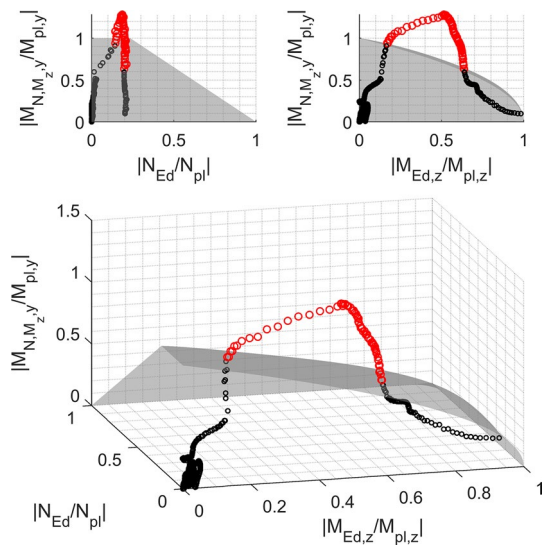


Fig. 27 NC— N - M_z - M_y Interaction domain according to Eurocode 3-1-1



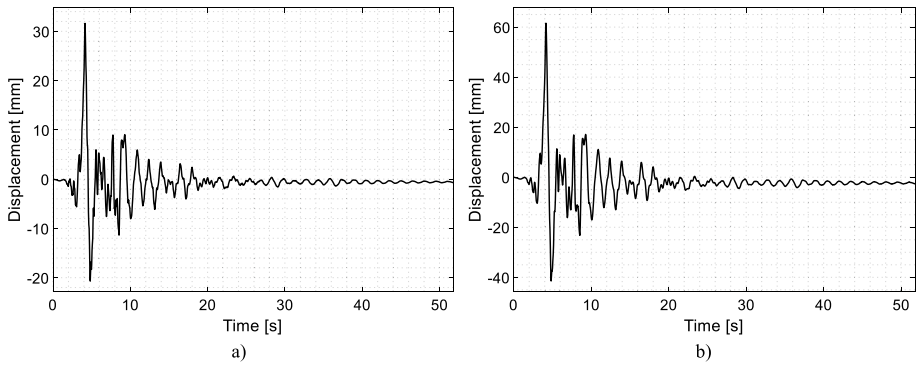


Fig. 28 NC—Actuator displacements: **a** Actuator 1, **b** Actuator 2

an out-of-plane rotation of the RBSs was detected, mainly caused by inherent imperfections of the specimen and in the load application point. For this reason, in the Near Collapse limit state test, additional displacement transducers were installed on RBSs 9 and 11 to quantify the extent of such a phenomenon.

6.3 Near collapse limit state

A strong nonlinearity characterised the structural behaviour at the NC limit state. The moment-rotation diagram reported in Fig. 24 demonstrates that the RBSs underwent significant plastic deformation, with a residual rotation of about 5 mrad. Moreover, strength reduction can be noticed from the experimental cycles. This is due to the interaction between the bending moment along the strong axis M_y and the bending moment along the weak axis M_z . As shown in Fig. 25, the displacement at the top flange of RBS n°10 is different between the two edges, highlighting the presence of an out-of-plane rotation. The time history of the estimated bending moments M_y and M_z is reported in Fig. 26, where the resisting plastic bending moments along the two axes were computed by neglecting the mutual interaction. Even in this case, the maximum value of both M_y and M_z exceeded the plastic resistance. In Fig. 27 the evolution of the (M_z, N, M_y) state/history for the hybrid simulation test at NC limit state is compared with the interaction domain, as defined in Eurocode 3-1-1 (CEN 2005c). For clarity, the points outside the safe domain are reported in red. It is important to note that, despite the use of the lateral beams to transfer the displacements to the specimen nodes, an axial force was detected in the beam links. Nevertheless, as shown in Fig. 27, this force is small, i.e. less than 20% of the axial plastic resistance. Moreover, it is interesting to note that after the first yielding, the second one occurred for bending along the weak axis (M_z), involving a very low value of M_y . This suggests that strength degradation observed in the experimental cycles is obtained mainly due to the M_y – M_z interaction.

Concerning the displacement of the two actuators, reported in Fig. 28, the maximum displacement achieved at the floor level was 31.61 mm, which corresponds to an interstorey drift ratio (IDR) of 0.90%. Figure 29 shows the bending moment history at the base of the first column, highlighting that it did not exceed the plastic limit even at the NC limit state test. This emphasises the protection that the devices provide to the structure in case of higher earthquake intensity than the design one. In addition, a residual interstorey drift of

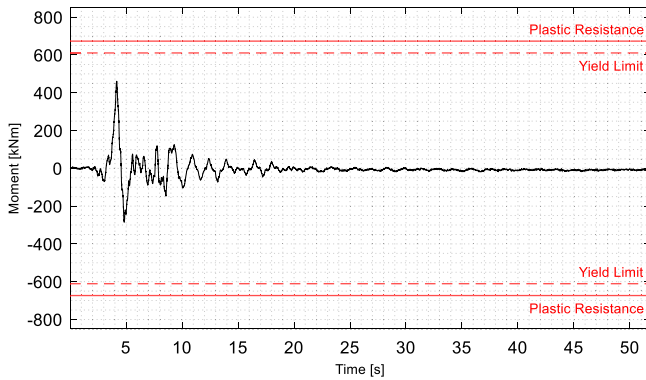
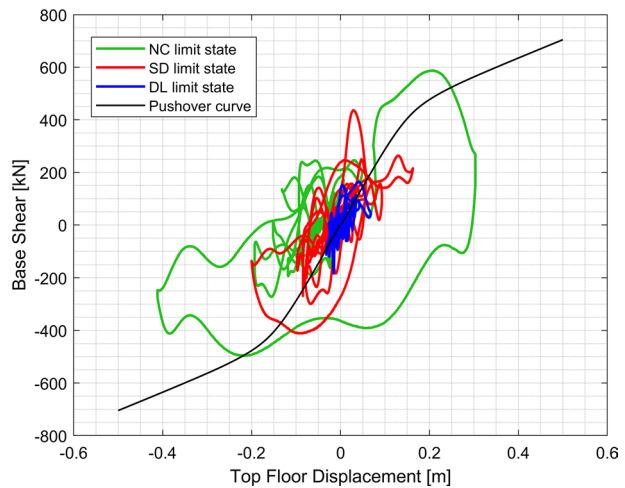


Fig. 29 NC—Bending moment at the base of the first column

Fig. 30 Base shear vs. Top floor displacement at the three limit states



0.03% was recorded, demonstrating the structure's re-centring capability and, as an important outcome, the ease of repair of the innovative frame even after undergoing NC limit state earthquake actions. Figure 30 reports the base shear vs top floor displacement for the three limit states. The three diagrams are superimposed with the pushover curve. Regarding the limit states, it should be noted that the structure remained in the elastic field for the DL limit state, while inelastic behaviour was observed for both the SD and NC limit states.

7 Calibration of the RBS nonlinear spring

After the tests, the nonlinear model of the DRLF component was calibrated on the experimental results using the Multical tool. The estimation of the stiffness parameters, needed for calibration, was based on three reliable RBSs hysteretic loops at the Near Collapse limit state, as shown in Fig. 31. For each loop, an elastic and hardening stiffness were evaluated for both the positive and negative branches. The stiffness values

Fig. 31 Elastic and hardening stiffness calibration on near collapse cycles

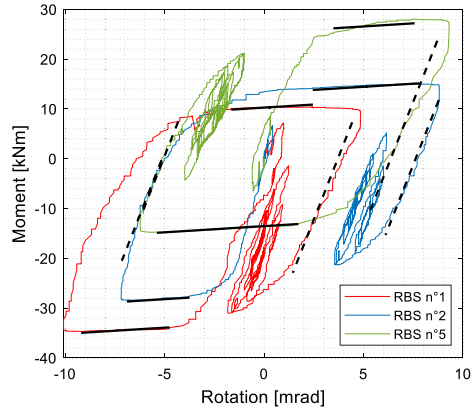


Table 12 Estimated stiffness parameters

Elastic stiffness K_{el} (kNm/rad)	1.01×10^4
Hardening stiffness K_{ha} (kNm/rad)	2.48×10^2
Hardening ratio (%)	2.45

Table 13 Calibrated Bouc–Wen parameters

Parameter		IPE160	
α (%)	2.45	β (-)	7.07×10^{12}
k (Nm/rad)	1.01×10^7	A (-)	1
n (-)	5	η (-)	0.0
γ (-)	7.07×10^{12}	ν (-)	0.0

Table 14 NRMSE between the test and the calibrated model results

	DL NRMSE (%)	SD NRMSE (%)	NC NRMSE (%)
<i>Displacement</i>			
Top floor	18.21	11.00	4.15
Actuator 1	14.66	11.29	11.97
Actuator 2	15.46	11.96	12.29
<i>Force</i>			
Base	16.42	12.42	6.74
Actuator 1	18.51	12.73	6.73

were determined considering the linear part of the cycles for both elastic and plastic ranges. Despite the experimental behaviour of the RBSs was affected by those of the numerical substructure, this effect was limited given the fact that the elastic and the hardening stiffness are independent of the loading history.

Figure 31, shows the calibrated stiffness values, defined as the mean value of the elastic and hardening stiffness of each hysteretic loop, as reported in Table 12. The mean values were employed to calibrate the model by fixing these parameters on

Multical and using the tool to calibrate the Bouc–Wen model's additional parameters, which are detailed in Table 13. Both strength and stiffness degradation were not considered in the calibration since it was impossible to separate the contribution of out-of-plane effects from that of the material's own degradation.

Following the calibration, time-history analyses on the updated model were carried out using the same set of ground motion records employed for the Hybrid Simulation. The results of the calibrated and experimental outcomes are compared in Table 14, where the NRMSE parameters in terms of displacement and forces are listed. The NRMSE parameter did not exceed 20%, revealing that a satisfactory agreement was achieved.

8 Conclusions

This article thoroughly described the results of a series of experimental tests performed on a full-scale steel frame equipped with DRLF components. Through the implementation of the partitioned $G-\alpha$ algorithm, Hybrid Simulation technique was successfully employed to characterise the seismic behaviour of the entire frame at three different limit states, namely, DL, SD and NC. Only the ground floor was physically built, whereas the remainder of the structure was numerically simulated. This enabled laboratory costs to be limited while simulating the full-scale structure response. The experimental behaviour satisfied the design assumptions, showing that all structural elements remained at the DL limit state in the elastic field. Only the DRLF links underwent significant plastic deformation at the SD limit state, resulting in large hysteretic loops, whilst the irreplaceable parts remained in the elastic range. Non-negligible out-of-plane behaviour of the DRLF components was observed with consequent bending interaction in the two principal axes, especially regarding the DRLF beam links at the NC limit state. Moreover, the DRLF system allowed for small residual lateral displacement, highlighting an excellent self-centring capability. In terms of repairability, it took 6 man/h to replace the components, which represents a beneficial outcome in the context of structural resilience. At the NC limit state, no damage was detected on the irreplaceable parts, i.e., beams, columns and joints, whilst the RBSs of the DRLF system experienced large plastic deformations, with residual plastic rotation. Since the structure was designed for the SD limit state, the protection given by the components to the irreplaceable elements at the NC limit state is a notable outcome of the experimental campaign. Finally, the numerical nonlinear behaviour of the RBSs was calibrated according to the moment-rotation cycle obtained from the NC limit state. The Finite Element model of the structure was subsequently updated, and the model results were compared with the experimental response, demonstrating a satisfactory agreement. Future perspectives include the employment of the calibrated components for numerical applications, e.g., Incremental Dynamic Analyses and seismic fragility curves.

Acknowledgements This project has received funding from the Research Fund for Coal and Steel under grant agreement No 800699. Views and opinions expressed are however those of the author(s) only and do not necessarily reflect those of the European Union or Research Fund for Coal and Steel. Neither the European Union nor the Research Fund for Coal and Steel can be held responsible for them. The research leading to these results has also received funding from the Italian Ministry of Education, Universities and Research (MUR) in the framework of the project DICAM-EXC (Departments of Excellence 2023–2027, grant L232/2016).

Author contributions Giulia Giuliani: Methodology, Software, Validation, Data processing, Writing – original draft. Roberto Andreotti: Methodology, Software, Data processing, Writing – review & editing. Nicola Tondini: Conceptualization, Methodology, Supervision, Writing – review & editing, Funding acquisition. All authors read and approved the final manuscript.

Funding Open access funding provided by Università degli Studi di Trento within the CRUI-CARE Agreement. This project has received funding from the Research Fund for Coal and Steel under grant agreement No 800699. Views and opinions expressed are however those of the author(s) only and do not necessarily reflect those of the European Union or Research Fund for Coal and Steel. Neither the European Union nor the Research Fund for Coal and Steel can be held responsible for them. The research leading to these results has also received funding from the Italian Ministry of Education, Universities and Research (MUR) in the framework of the project DICAM-EXC (Departments of Excellence 2023–2027, grant L232/2016).

Declarations

Conflict of interests The authors have no relevant financial or non-financial interests to disclose.

Data availability Data will be made available on request.

Open Access This article is licensed under a Creative Commons Attribution 4.0 International License, which permits use, sharing, adaptation, distribution and reproduction in any medium or format, as long as you give appropriate credit to the original author(s) and the source, provide a link to the Creative Commons licence, and indicate if changes were made. The images or other third party material in this article are included in the article's Creative Commons licence, unless indicated otherwise in a credit line to the material. If material is not included in the article's Creative Commons licence and your intended use is not permitted by statutory regulation or exceeds the permitted use, you will need to obtain permission directly from the copyright holder. To view a copy of this licence, visit <http://creativecommons.org/licenses/by/4.0/>.

References

- Abbiati G, Bursi OS, Caperan P, Di Sarno L, Molina FJ, Paolacci F, Pegon P (2015) Hybrid simulation of a multi-span RC viaduct with plain bars and sliding bearings. *Earthq Eng Struct Dynam* 44:2221–2240. <https://doi.org/10.1002/eqe.2580>
- Abbiati G, Covi P, Tondini N, Bursi OS, Stojadinović B (2020) A real-time hybrid fire simulation method based on dynamic relaxation and partitioned time integration. *J Eng Mech* 146:04020104. [https://doi.org/10.1061/\(ASCE\)EM.1943-7889.0001826](https://doi.org/10.1061/(ASCE)EM.1943-7889.0001826)
- Abbiati G, Lanese I, Cazzador E, Bursi OS, Pavese A (2019) A computational framework for fast-time hybrid simulation based on partitioned time integration and state-space modeling. *Struct Control Health Monit* 26. <https://doi.org/10.1002/stc.2419>
- Abbiati G (2014) Dynamic substructuring of complex hybrid systems based on time-integration, model reduction and model identification techniques (PhD Thesis). University of Trento.
- Andreotti R, Giuliani G, Tondini N (2023a) Experimental analysis of a full-scale steel frame with replaceable dissipative connections. *J Constr Steel Res* 208:108036. <https://doi.org/10.1016/j.jcsr.2023.108036>
- Andreotti R, Giuliani G, Tondini N, Bursi OS (2023b) Hybrid simulation of a partial-strength steel–concrete composite moment-resisting frame endowed with hysteretic replaceable beam splices. *Earthq Eng Struct Dynam* 52:51–70. <https://doi.org/10.1002/eqe.3744>
- Bonelli A, Bursi OS (2005) Predictor-corrector procedures for pseudo-dynamic tests. *Eng Comput* 22:783–834. <https://doi.org/10.1108/02644400510619530>
- Bouc R (1967) Forced vibrations of mechanical systems with hysteresis. In: Presented at the fourth conference on nonlinear oscillations, Prague
- Bursi OS, Wagg D (2009) Modern testing techniques for structural systems: dynamics and control. CISM International Centre for Mechanical Sciences. Springer Science & Business Media
- Castiglioni CA, Dougka G, Kalteziotis D, Karydakis Ph, Calado L, Kanyilmaz A, Vayas I, Proença JM, Hoffmeister B, Rauert T, Dimakogianni D, Espinha M (2013) Dissipative devices for seismic-resistant steel frames (Fuseis), European Commission. Publications Office, LU, Directorate General for Research and Innovation
- Castro J, Elghazouli A, Izzuddin B (2005) Modelling of the panel zone in steel and composite moment frames. *Eng Struct* 27:129–144. <https://doi.org/10.1016/j.engstruct.2004.09.008>
- CEN (European Committee for Standardization) (2005a) Eurocode 8: design of structures for earthquake resistance—Part 1: General rules, seismic actions and rules for buildings
- CEN (European Committee for Standardization) (2005b) Eurocode 8: design of structures for earthquake resistance—Part 3: Assessment and retrofitting of buildings

- CEN (European Committee for Standardization) (2005c) Eurocode 3: design of steel structures—Part 1–1: General rules and rules for buildings
- CEN (European Committee for Standardization) (2018) Eurocode 8: design of structures for earthquake resistance—Part 1: general rules, seismic actions and rules for buildings. Working draft
- Chan RW, Albermani F (2008) Experimental study of steel slit damper for passive energy dissipation. *Eng Struct* 30:1058–1066. <https://doi.org/10.1016/j.engstruct.2007.07.005>
- Chen S-J, Yeh CH, Chu JM (1996) Ductile steel beam-to-column connections for seismic resistance. *J Struct Eng* 122:1292–1299. [https://doi.org/10.1061/\(ASCE\)0733-9445\(1996\)122:11\(1292\)](https://doi.org/10.1061/(ASCE)0733-9445(1996)122:11(1292))
- Chisari C, Francavilla AB, Latour M, Piluso V, Amadio C (2017) Critical issues in parameter calibration of cyclic models for steel members. *Eng Struct* 123–138. <https://doi.org/10.1016/j.engstruct.2016.11.030>
- CSI C, S. Inc. (2019) SAP2000 integrated software for structural analysis and design
- Del Carpio Ramos M, Mosqueda G, Hashemi MJ (2016) Large-scale hybrid simulation of a steel moment frame building structure through collapse. *J Struct Eng* 142:04015086. [https://doi.org/10.1061/\(ASCE\)ST.1943-541X.0001328](https://doi.org/10.1061/(ASCE)ST.1943-541X.0001328)
- Di Benedetto S, Francavilla AB, Latour M, Ferrante Cavallaro G, Piluso V, Rizzano G (2020) Pseudodynamic testing of a full-scale two-storey steel building with RBS connections. *Eng Struct* 212:110494. <https://doi.org/10.1016/j.engstruct.2020.110494>
- Dusicka P, Iwai R (2007) Development of linked column frame system for seismic lateral loads. In: Presented at the research frontiers at structures congress 2007, American Society of Civil Engineers, Long Beach, California, USA, pp 1–13. [https://doi.org/10.1061/40944\(249\)63](https://doi.org/10.1061/40944(249)63)
- Flores F, Charney F, Lopez-Garcia D (2016) The influence of gravity column continuity on the seismic performance of special steel moment frame structures. *J Constr Steel Res* 118:217–230. <https://doi.org/10.1016/j.jcsr.2015.11.010>
- Fortney PJ, Shahrooz BM, Rassati GA (2007) Large-scale testing of a replaceable “Fuse” steel coupling beam. *J Struct Eng* 133:1801–1807. [https://doi.org/10.1061/\(ASCE\)0733-9445\(2007\)133:12\(1801\)](https://doi.org/10.1061/(ASCE)0733-9445(2007)133:12(1801))
- Francavilla AB, Latour M, Piluso V, Rizzano G (2020) Design criteria for beam-to-column connections equipped with friction devices. *J Constr Steel Res* 172:106240. <https://doi.org/10.1016/j.jcsr.2020.106240>
- Hess PE, Bruchman D, Assakkaf IA, Ayyub BM (2002) Uncertainties in material and geometric strength and load variables. *Nav Eng J* 114:139–166. <https://doi.org/10.1111/j.1559-3584.2002.tb00128.x>
- Iwankiw NR, Carter CJ (1996) The dogbone: a new idea to chew on. *Mod Steel Constr* 36(4):18–23
- Kanyilmaz A, Kondratenko A, Castiglioni CA, Calado L, Proença JM, Mouzakis H, Psycharis I, Thanopoulos P, Papavasileiou K, Sofras M, Tondini N, Andreotti R, Giuliani G, Bonelli A, Bursi OS, Vulcu C, Pinkawa M, Hoffmeister B, Rocco E, Napolano L, Zilli G, Caprili S, Panzera I, Mattei F, Salvatore W (2022) Fully dissipative and easily repairable components for resilient buildings with composite steel-concrete structures. European Commission Project Number 800699
- Latour M, Piluso V, Rizzano G (2011) Experimental analysis of innovative dissipative bolted double split tee beam-to-column connections. *Steel Constr* 4:53–64. <https://doi.org/10.1002/stco.201110009>
- Li J, Spencer BF, Elnashai AS, Phillips BM (2012) Substructure hybrid simulation with multiple-support excitation. *J Eng Mech* 138:867–876. [https://doi.org/10.1061/\(ASCE\)EM.1943-7889.0000394](https://doi.org/10.1061/(ASCE)EM.1943-7889.0000394)
- Lopes A, Dusicka P, Berman J (2012) Linked column framing system analyses toward experimental validation. In: Presented at the structures congress 2012, American Society of Civil Engineers, Chicago, IL, pp 1598–1609. <https://doi.org/10.1061/9780784412367.142>
- Lopes A, Dusicka P, Berman J (2014) Linked column frame steel system performance validation using hybrid simulation. In: Presented at the tenth US national conference on earthquake engineering, Anchorage, Alaska
- Malakoutian M, Berman JW, Dusicka P (2013) Seismic response evaluation of the linked column frame system. *Earthq Engng Struct Dyn* 42:795–814. <https://doi.org/10.1002/eqe.2245>
- Mazzolani F, Piluso V (1996) Theory and design of seismic resistant steel frames. CRC Press, London
- McKenna F, Fenves G, Scott M (2006) OpenSees: open system for earthquake engineering simulation. University of California Berkeley
- Ministero dei Lavori Pubblici (1996) Norme tecniche per il calcolo, l'esecuzione ed il collaudo delle strutture in cemento armato normale e precompresso e per le strutture metalliche
- Montuori R, Nastro E, Piluso V, Pisapia A (2023) Design procedure for failure mode control of linked column frames. *Eng Struct* 296:116937. <https://doi.org/10.1016/j.engstruct.2023.116937>
- Nakashima M (2020) Hybrid simulation: an early history. *Earthq Eng Struct Dynam* 49:949–962. <https://doi.org/10.1002/eqe.3274>
- Oh S-H, Kim Y-J, Ryu H-S (2009) Seismic performance of steel structures with slit dampers. *Eng Struct* 31:1997–2008. <https://doi.org/10.1016/j.engstruct.2009.03.003>

- Pastor M, Binda M, Harčarik T (2012) Modal assurance criterion. *Proc Eng* 48:543–548. <https://doi.org/10.1016/j.proeng.2012.09.551>
- Pinkawa M, Bartsch H, Schaffrath S, Hoffmeister B, Feldmann M (2017) Seismic design of steel frames with fuseis beam link energy dissipation systems. Rhodes Island, pp 878–890. <https://doi.org/10.7712/120117.5463.18111>
- Plumier A, Doneux C, Castiglioni CA (2006) Two innovations for earthquake-resistant design: the INERD project: final report, European Commission, Directorate General for Research and Innovation. Publications Office
- Plumier A (1990) New idea for safe structures in seismic zones IABSE Symposium-Mixed Structures Including New Materials. <https://doi.org/10.5169/SEALS-46518>
- Pucinotti R, Tondini N, Zanon G, Bursi OS (2015) Tests and model calibration of high-strength steel tubular beam-to-column and column-base composite joints for moment-resisting structures: high-strength steel tubular beam-to-column and column-base composite joints. *Earthq Eng Struct Dynam* 44:1471–1493. <https://doi.org/10.1002/eqe.2547>
- Sauca A, Gernay T, Robert F, Tondini N, Franssen J-M (2018) Hybrid fire testing: discussion on stability and implementation of a new method in a virtual environment. *JSFE* 9:319–341. <https://doi.org/10.1108/JSFE-01-2017-0017>
- Smith, M., 2009. ABAQUS/Standard User's Manual.
- Tondini N, Zanon G, Pucinotti R, Di Filippo R, Bursi OS (2018) Seismic performance and fragility functions of a 3D steel-concrete composite structure made of high-strength steel. *Eng Struct* 174:373–383. <https://doi.org/10.1016/j.engstruct.2018.07.026>
- Valente M, Castiglioni CA, Kanyilmaz A (2016) Dissipative devices for earthquake resistant composite steel structures: bolted versus welded solution. *Bull Earthq Eng* 14:3613–3639. <https://doi.org/10.1007/s10518-016-0002-9>
- Vayas I (2017) Innovative anti-seismic devices and systems: INNOSEIS Project RFCS-02-2015, 1st edn. ECCS, Zürich
- Wang M, Dong K, Liu M (2020) Damage control mechanism and seismic performance of a steel moment connection with replaceable low-yield-point steel double T-stub fuses. *Thin-Walled Struct* 157:107143. <https://doi.org/10.1016/j.tws.2020.107143>
- Wen Y-K (1976) Method for random vibration of hysteretic systems. *J Eng Mech Div* 102:249–263. <https://doi.org/10.1061/JMCEA3.0002106>

Publisher's Note Springer Nature remains neutral with regard to jurisdictional claims in published maps and institutional affiliations.